# HDO and SO2 thermal mapping on Venus: VI. Anomalous SO2 behavior during late 2021

Thérèse Encrenaz, Thomas K. Greathouse, Rohini S. Giles, Thomas Widemann, Bruno Bézard, Maxence Lefevre, Wencheng D. Shao

A&A 674, A199 (2023)
https://doi.org/10.1051/0004-6361/202245831


Astronomy & Astrophysics

# HDO and $SO_2$ thermal mapping on Venus

## VI. Anomalous $SO_2$ behavior during late 2021

T. Encrenaz[1], T. K. Greathouse[2], R. Giles[2], T. Widemann[1], B. Bézard[1], M. Lefèvre[3], and W. Shao[4]

[1] LESIA, Observatoire de Paris, PSL University, CNRS, Sorbonne Université, Université de Paris, 92195 Meudon, France
e-mail: therese.encrenaz@obspm.fr
[2] Space Science Department, Southwest Research Institute, Div. 15, San Antonio, TX 78228, USA
[3] LATMOS/IPSL, UVSQ Université Paris-Saclay, Sorbonne Université, CNRS, 78280 Guyancourt, France
[4] Dept. of Earth and Planetary Sciences, University of California, Santa Cruz, CA 95064, USA

Received 31 December 2022 / Accepted 28 March 2023

**ABSTRACT**

Since January 2012, we have been monitoring the behavior of sulfur dioxide and water on Venus using the Texas Echelon Cross-Echelle Spectrograph (TEXES) imaging spectrometer at the NASA InfraRed Telescope Facility (IRTF, Mauna Kea Observatory). We present here new data recorded in 2021 and 2022, after an 18-month interruption due to the Covid pandemic. Most of the observations were recorded in two spectral ranges: the 7.4 μm (1345 $cm^{-1}$) range, where $SO_2$, $CO_2$, and HDO (used as a proxy for $H_2O$) transitions are observed at the cloud top, at an altitude of about 62 km, and the 19 μm (530 $cm^{-1}$) range, where $SO_2$ and $CO_2$ are probed within the clouds at an altitude of about 57 km. We recently added the 8.6 μm (1162 $cm^{-1}$) range, which probes a few kilometers above the cloud top ($z$ = 67 km). As in our previous studies, the volume mixing ratio of $SO_2$ is estimated using the $SO_2/CO_2$ line depth ratio of weak transitions; the $H_2O$ volume mixing ratio is derived from the HDO/$CO_2$ line depth ratio, assuming a D/H ratio of 200 times the Vienna Standard Mean Ocean Water (VSMOW). As reported in our previous analyses, the $SO_2$ mixing ratio shows strong variations with time and also over the disk, showing evidence of the formation of $SO_2$ plumes. These local maxima appear sporadically on the $SO_2$ maps and stay visible over a few hours. In contrast, the $H_2O$ abundance is remarkably uniform over the disk and shows moderate variations as a function of time. The present dataset shows significant differences with respect to the 2012–2019 dataset: (1) the $SO_2$ mixing ratio at the cloud top has decreased by a factor of about 3 with respect to the maximum value observed in July 2018; (2) the long-term anti-correlation between $SO_2$ and $H_2O$ previously observed between 2014 and 2019 is no longer visible; (3) a very high $SO_2$ plume activity was observed in Nov. 2021, in spite of the low $SO_2$ mixing ratio at the cloud top. In contrast, the distribution of the $SO_2$ plume appearance over the disk is confirmed, with a maximum along the equator and around the morning terminator. Information on the $SO_2$ vertical gradient is retrieved from the simultaneous analysis of $SO_2$ at 7.4 μm and 19 μm. The gradient is constant in most cases with a few exceptions, especially in November 2021 when the plume activity was high. Finally, the temperature distributions retrieved from the continuum maps in September and November 2021 show an unusual pattern possibly associated with gravity waves, as previously observed by the longwave infrared camera camera aboard the Akatsuki spacecraft.

**Key words.** planets and satellites: atmospheres – planets and satellites: composition – planets and satellites: terrestrial planets

## 1. Introduction

Water and sulfur dioxide are the drivers of the atmospheric chemistry of Venus (Krasnopolsky 1986, 2007, 2010; Mills et al. 2007; Zhang et al. 2012). Below the clouds, both species are present with relatively high abundances (about 30 ppmv and 130 ppmv respectively; Bézard & De Bergh 2012; Marcq et al. 2018) and, at low latitudes, are transported upward by Hadley convection. Following the $SO_2$ photodissociation and the combination of $SO_3$ with $H_2O$, sulfuric acid $H_2SO_4$ is formed and condenses as the main component of the cloud deck. Above the cloud top, the volume mixing ratios (vmr) of $H_2O$ and $SO_2$ drop drastically to about 1–3 ppmv (Fedorova et al. 2008; Belyaev et al. 2012) and 10–1000 ppbv (Zasova et al. 1993; Marcq et al. 2013; Markiewicz et al. 2007; Vandaele et al. 2017a,b), respectively.

The two species have been extensively monitored over several decades, with Pioneer Venus, the Venera 15 spacecraft, Venus Express, and Akatsuki using imaging and spectroscopy in the ultraviolet and infrared ranges. As a complement to these datasets, since 2012 we have been using ground-based imaging spectroscopy in the thermal infrared to map $SO_2$ and $H_2O$ at the cloud top of Venus and to monitor the behavior of these two species as a function of time. Thirteen runs have been recorded between 2012 and 2019 (Encrenaz et al. 2012, 2013, 2016, 2019, 2020, hereafter E12, E13, E16, E19, and E20). The main result of these studies is that $SO_2$ and $H_2O$ were found to exhibit very different behaviors. $H_2O$ is always uniformly distributed over the disk and shows moderate variations on the long term; in contrast, the $SO_2$ maps most often show sporadic plumes (i.e., local maxima that appear and disappear on a typical timescale of a few hours). During their lifetime, they follow the four-day rotation of the clouds at the cloud top. The disk-integrated $SO_2$ abundance also shows strong variations over the long term, with a contrast factor of about 10 between the minimum value observed in February 2014 and the maximum value of July 2018.

After an 18-month interruption due to the Covid pandemic, five new observing runs were obtained in June, September, and November 2021, and in February and June 2022. In this paper

**Table 1.** Summary of TEXES runs in 2021 and 2022.

| Date of obs. | Venus diameter (arcsec) | Morning/evening | SEP longitude (degrees) | SSP longitude range (degrees) |
|---|---|---|---|---|
| 2021/06/26–2021/07/07 | 12–11 | Evening | 223–266 | 255–308 |
| 2021/09/26–2021/10/02 | 18–19 | Evening | 124–139 | 197–216 |
| 2021/11/06–2021/11/11 | 26–29 | Evening | 228–240 | 323–339 |
| 2022/02/25–2022/03/04 | 33–31 | Morning | 57–68 | 310–328 |
| 2022/06/24–2022/07/04 | 12–11 | Morning | 1–29 | 315–346 |

**Notes.** SEP and SSP are the sub-Earth point and the sub-solar point, respectively.

we describe these observations in Sect. 2. Then in Sect. 3 we use the whole Texas Echelon Cross-Echelle Spectrograph (TEXES) dataset (2012–2022) at 7.4 μm to study the long-term evolution of $H_2O$ and $SO_2$. In Sect. 4 we update our statistical analysis of the $SO_2$ plumes, regarding their appearance as a function of latitude, longitude, and local hour. In Sect. 5 we present in more detail the temperature maps and the $SO_2$ maps obtained in September and November 2021, which exhibit an unusual behavior. In a search of the origin of this behavior, in Sect. 6 we present an analysis of the long-term variations in the plume activity and, using both the 7 μm and the 19 μm datasets, the long-term variations in the $SO_2$ vertical gradient in the few kilometers below the cloud top. The results are discussed and our conclusions are summarized in Sect. 7.

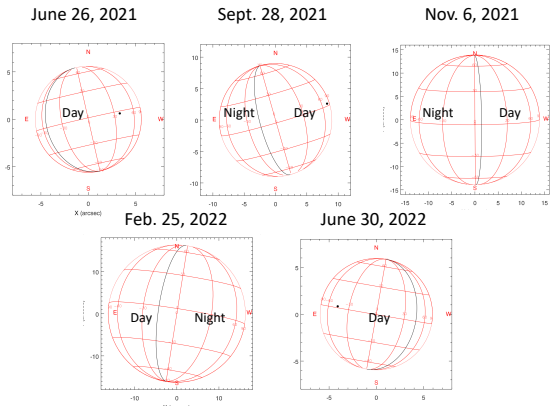


**Fig. 1.** Geometrical configurations of the disk of Venus during the five TEXES runs of 2021 and 2022. The terminator is indicated with a black line and the sub-solar point with a black dot.

## 2. The data

The Texas Echelon Cross Echelle Spectrograph (TEXES) is an imaging high-resolution thermal infrared spectrometer in operation at the NASA InfraRed telescope Facility (Lacy et al. 2002), which combines high spectral ($R$ = 80 000 at 7 μm) and spatial (around 1 arcsec) capabilities. As for our previous observations, we selected three spectral ranges: the 1342–1348 $cm^{-1}$ (7.4 μm) interval, the 529–530 $cm^{-1}$ (19 μm) interval, and the 1160–1165 $cm^{-1}$ (8.6 μm) interval. The first interval (7.4 μm) has been used regularly since 2012 to monitor the mixing ratios of $SO_2$ and HDO at the cloud top ($z$ = 62 km). The second interval (19 μm) has also been used regularly to monitor the $SO_2$ abundance a few kilometers below the cloud top ($z$ = 57 km). The third interval (8.6 μm) probes a few kilometers above the cloud top ($z$ = 67 km) and also contains the weak $\nu_1$ band of $SO_2$. This band is difficult to detect on Venus, both because of its intrinsic weakness and because the sharp depletion of $SO_2$ above the cloud top (E13). However, when the $SO_2$ abundance at the cloud top is high (as in 2018 and 2019), the band might be detectable or its absence might bring a constraint on the $SO_2$ vertical gradient above the clouds. For this reason we have observed this spectral range regularly since June 2021.

Five runs took place in 2021 and 2022 (June–July 2021, September–October 2021, November 2021, February–March 2022, June–July 2022); the observing parameters are listed in Table 1. Figure 1 shows the geometrical configurations of the five runs. The evening terminator was observed in 2021, and the morning terminator in 2022. The length and the width of the slit were respectively 6.0 and 1.0 arcsec at 7.4 μm, 12.0 and 2.0 arcsec at 19 μm, and 8.0 and 1.0 arcsec at 8.6 μm. As we did previously, we aligned the slit along the north–south celestial axis and we shifted it from west to east, with a step of half the slit width and an integration time of two seconds per position, to cover the planet in longitude from limb to limb, and to add a few pixels on the sky beyond each limb for sky subtraction. Since the rotation axis of Venus is close to the celestial axis, each scan corresponds to a given latitude range of about 6 arcsec. As the diameter of Venus was always larger than the slit length, we multiplied the scans to cover the full latitude range from north to south with some overlap. Tables 2–4 summarize the TEXES observations recorded in 2021 and 2022. These tables list the maps obtained in all three spectral ranges with, in each case, the start time of the map.

The TEXES data cubes were calibrated using the standard radiometric method (Lacy et al. 2002; Rohlfs & Wilson 2004). Calibration frames consisting of three measurements (black chopper blade, sky, and low-emissivity chopper blade) are systematically taken before each observing scan, and the difference (black-sky) is taken as a flat field. If the temperature of the black blade, the telescope, and the sky are equal, this method corrects both telescope and atmospheric emissions. The atmospheric correction, however, is not complete for all terrestrial atmospheric lines, partly because these lines are not all formed at the same atmospheric levels, and thus have different temperatures. For these reasons, as in the case of our previous analyses, we do not try to correct the terrestrial atmospheric features and we select $SO_2$ and $CO_2$ lines located outside these features.

**Table 2.** Summary of TEXES observations recorded from June to November 2021.

| Date of obs. | Spectral range (cm-1) | Map | Start time (UT) |
|---|---|---|---|
| 2021/06/26 | 1345 | a | 20:35:48 |
| 2021/06/26 | 530 | a | 20:57:40 |
| 2021/06/26 | 1162 | a | 21:38:39 |
| 2021/06/26 | 1345 | b | 22:28:32 |
| 2021/06/26 | 530 | b | 22:52:58 |
| 2021/06/26 | 1162 | b | 23:07:04 |
| 2021/06/26 | 1345 | c | 23:45:00 |
| 2021/06/26 | 530 | c | 00:17:14 |
| 2021/07/07 | 1345 | | 21:18:51 |
| 2021/07/07 | 530 | | 21:34:07 |
| 2021/07/07 | 1162 | | 21:48:32 |
| 2021/09/26 | 1345 | | 02:08:51 |
| 2921/09/26 | 530 | | 02:38:59 |
| 2021/09/26 | 1162 | | 03:03:44 |
| 2021/09/27 | 1345 | a | 00:31:20 |
| 2021/09/27 | 530 | a | 00:58:27 |
| 2021/09/27 | 1345 | b | à1:56:59 |
| 2021/09/27 | 530 | b | 02:23:21 |
| 2021/09/28 | 1345 | a | 23:47:16 |
| 2021/09/28 | 530 | a | 01:46:52 |
| 2021/09/28 | 1345 | b | 01:21:14 |
| 2021/09/28 | 530 | b | 01:46:52 |
| 2021/09/29 | 1345 | a | 23:25:12 |
| 2021/09/29 | 530 | a | 23:51:39 |
| 2021/09/29 | 1345 | b | 00:59:52 |
| 2021/09/29 | 530 | b | 01:27:12 |
| 2021/09/30 | 1345 | | 02:39:37 |
| 2021/09/30 | 530 | | 03:07:23 |
| 2021/09/30 | 1162 | | 03:23:54 |
| 2021/10/02 | 1345 | | 03:25:33 |
| 2021/11/06 | 1345 | a | 22:43:12 |
| 2021/11/06 | 1345 | b | 23:43:05 |
| 2021/11/06 | 530 | | 00:33:15 |
| 2021/11/06 | 1162 | | 01:26:47 |
| 2021/11/07 | 1345 | a | 23:45:23 |
| 2021/11/07 | 1162 | | 01:20:31 |
| 2021/11/07 | 1345 | b | 03:37:10 |
| 2021/11/08 | 1345 | a | 23:44:18 |
| 2021/11/08 | 1345 | b | 02:22:36 |
| 2021/11/09 | 1345 | | 00:34:10 |
| 2021/11/09 | 1162 | | 02:01:19 |
| 2021/11/10 | 1345 | | 00:12:24 |
| 2021/11/11 | 1345 | | 00:07:44 |
| 2021/11/11 | 530 | | 01:06:10 |
| 2021/11/11 | 1162 | | 01:46:34 |

**Notes.** When several maps were recorded the same day at a given frequency, a letter (a, b,...) has been added. The third column refers to the various maps (a, b, c) recorded each day at a given frequency.

**Table 3.** Summary of TEXES observations recorded in February–March 2022.

| Date | Spectral range | Map | Start time |
|---|---|---|---|
| 2022/02/25 | 1345 | a | 17:39:19 |
| 2022/02/25 | 530 | | 18:43:42 |
| 2022/02/25 | 1162 | | 20:51:07 |
| 2022/02/25 | 1345 | b | 21:48:17 |
| 2022/02/26 | 1345 | a | 17:19:06 |
| 2022/02/26 | 1345 | b | 20:36:08 |
| 2022/02/26 | 1345 | c | 22:16:28 |
| 2022/02/27 | 1345 | a | 17:28:01 |
| 2022/02/27 | 530 | | 18:32:22 |
| 2022/02/27 | 1162 | | 20:32:09 |
| 2022/02/27 | 1345 | b | 21:43:30 |
| 2022/02/28 | 1345 | a | 16:48:48 |
| 2022/02/28 | 1345 | b | 19:51:23 |
| 2022/02/28 | 530 | | 20:52:49 |
| 2022/02/28 | 1345 | c | 21:50:31 |
| 2022/03/01 | 1345 | a | 16:55:17 |
| 2022/03/01 | 530 | | 19:14:09 |
| 2022/03/01 | 1162 | | 20:20:56 |
| 2022/03/01 | 1345 | b | 21:52:17 |
| 2022/03/02 | 1345 | a | 17:35:22 |
| 2022/03/02 | 1345 | b | 20:55:06 |
| 2022/03/02 | 530 | | 21:52:26 |
| 2022/03/03 | 1345 | a | 17:53:22 |
| 2022/03/03 | 530 | | 20:10:33 |
| 2022/03/03 | 1162 | | 20:49:15 |
| 2022/03/03 | 1345 | b | 21:37:56 |

**Notes.** The third column refers to the various maps (a, b, c) recorded each day at a given frequency.

Figures 2 and 3 show representative disk-integrated spectra corresponding to the runs of 2021 and 2022 in the 7.4 and 19 μm range, respectively. The 7.3 μm spectral range (1344.8–1345.4 $cm^{-1}$) includes several weak $SO_2$ transitions, two weak $CO_2$ lines, and one weak HDO line. As in our previous studies (see E19), we used the HDO line at 1344.90 $cm^{-1}$, the $SO_2$ multiplet at 1345.1 $cm^{-1}$, and the $CO_2$ line at 1345.22 $cm^{-1}$ in order to retrieve the $H_2O$ and $SO_2$ mixing ratios directly from the line depth ratios (ldr). In the 19 μm range (529–530 $cm^{-1}$) weak transitions of $SO_2$ and $CO_2$ are found (E16). This spectral interval is not easy to observe because, due to instrumental constraints, the full spectrum cannot be recorded continuously from 529 to 530 $cm^{-1}$ (see E13; Fig. 7), and a choice has to be made about the $SO_2$ and $CO_2$ transitions to be used for retrieving the $SO_2$ vmr. In 2012, we used the $SO_2$ multiplet around 529.7 $cm^{-1}$ (E13) and, in subsequent studies, we used the $SO_2$ multiplet around 529.32 $cm^{-1}$ (E16). However, in 2021–2022, for technical reasons, this multiplet was not observed, and we again used the 529.7 $cm^{-1}$ $SO_2$ multiplet, associated with the $CO_2$ line at 529.81 $cm^{-1}$, for which the near continuum is easier to observe. It can be seen (Fig. 7 of E16) that the $SO_2/CO_2$ ldr inferred from these transitions is equal to that inferred from the 529.33 $cm^{-1}$ $SO_2$ multiplet and the 529.26 $cm^{-1}$ line of $CO_2$ used in our previous analysis. As can be seen in Fig. 3, the $SO_2$ transitions are

**Table 4.** Summary of TEXES observations recorded in June–July 2022.

| Date | Spectral range | Map | Start time |
|---|---|---|---|
| 2022/06/24 | 1345 | a | 17:53:11 |
| 2022/06/24 | 530 | a | 18:19:31 |
| 2022/06/24 | 1162 | | 18:47:11 |
| 2022/06/24 | 1345 | b | 19:31:24 |
| 2022/06/24 | 530 | a | 19:57:15 |
| 2022/06/25 | 1345 | a | 17:42:21 |
| 2022/06/25 | 530 | a | 18:07:25 |
| 2022/06/25 | 1345 | b | 18:48:35 |
| 2022/06/25 | 530 | b | 19:13:38 |
| 2022/06/25 | 1345 | c | 19:55:20 |
| 2022/06/25 | 1345 | d | 20:38:10 |
| 2022/06/26 | 1345 | a | 16:39:39 |
| 2022/06/26 | 530 | a | 17:09:05 |
| 2022/06/26 | 1345 | b | 18:23:19 |
| 2022/06/26 | 530 | b | 18:48:09 |
| 2022/06/26 | 1345 | c | 19: 34:21 |
| 2022/06/26 | 1345 | d | 20:42:44 |
| 2022/06/27 | 1345 | a | 18:39:06 |
| 2022/06/27 | 530 | a | 19:04:27 |
| 2022/06/27 | 1345 | b | 19:45:50 |
| 2022/06/27 | 530 | b | 20:06:27 |
| 2022/06/27 | 1345 | c | 20:36:17 |
| 2022/06/28 | 1345 | a | 17:56:49 |
| 2022/06/28 | 530 | a | 19:04:27 |
| 2022/06/28 | 1345 | b | 19:35:16 |
| 2022/06/28 | 530 | b | 20:00:53 |
| 2022/06/28 | 1345 | c | 20:42:51 |
| 2022/06/29 | 1345 | a | 16:33:21 |
| 2022/06/29 | 530 | a | 17:07:17 |
| 2022/06/29 | 1345 | b | 17:52:38 |
| 2022/06/29 | 530 | b | 18:19:35 |
| 2022/06/29 | 1345 | c | 18:38:32 |
| 2022/06/29 | 1345 | d | 19:27:04 |
| 2022/06/29 | 1345 | e | 20:13:47 |
| 2022/06/30 | 1345 | a | 16:46:56 |
| 2022/06/30 | 530 | a | 17:14:30 |
| 2022/06/30 | 1345 | b | 18:38:40 |
| 2022/06/30 | 1345 | c | 19:48:42 |
| 2022/07/01 | 1345 | a | 16:25:51 |
| 2022/07/01 | 530 | a | 16:52:24 |
| 2022/07/01 | 1345 | b | 17:42:25 |
| 2022/07/01 | 530 | b | 18:07:43 |
| 2022/07/01 | 1345 | c | 18:49:14 |
| 2022/07/01 | 1345 | d | 19:34:37 |
| 2022/07/02 | 1345 | a | 17:17:54 |
| 2022/07/02 | 530 | a | 17:43:22 |
| 2022/07/02 | 1345 | b | 18:50:34 |
| 2022/07/02 | 530 | b | 19:16:19 |
| 2022/07/03 | 1345 | a | 16:38:51 |
| 2022/07/03 | 530 | a | 17:06:23 |
| 2022/07/03 | 1345 | b | 17:49:29 |
| 2022/07/03 | 530 | b | 18:15:08 |
| 2022/07/03 | 1345 | c | 18:33:45 |
| 2022/07/03 | 1345 | d | 19:16:41 |
| 2022/07/03 | 1345 | e | 20:13:44 |
| 2022/07/04 | 1345 | a | 16:32:05 |
| 2022/07/04 | 1162 | | 17:18:23 |
| 2022/07/04 | 1345 | b | 17:36:03 |
| 2022/07/04 | 1345 | c | 18:56:22 |
| 2022/07/04 | 530 | | 19:15:20 |
| 2022/07/04 | 1345 | d | 20:27:32 |

**Notes.** The third column refers to the various maps (a–e) recorded each day at a given frequency.

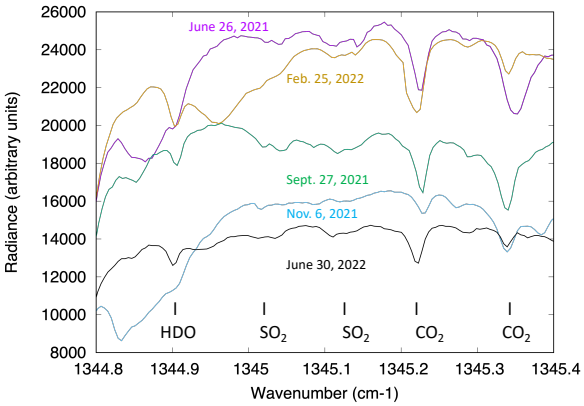


**Fig. 2.** Examples of disk-integrated spectra of Venus between 1344.8 and 1345.4 $cm^{-1}$ (7.4 µm) recorded in 2021 and 2022. The absorption feature around 1344.84 $cm^{-1}$ is due to terrestrial absorption and varies from day to day. The signal-to-noise ratio in each spectrum is above 1000, so the error bars are not visible.

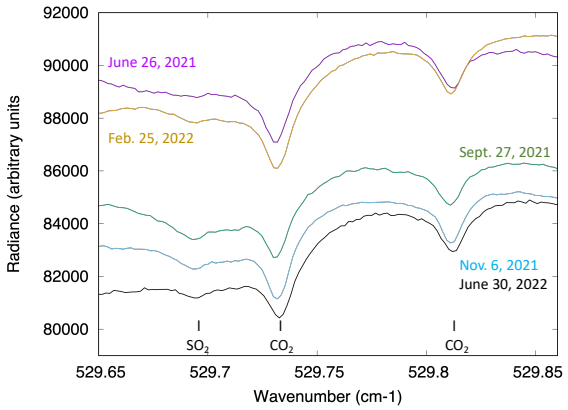


**Fig. 3.** Examples of disk-integrated spectra of Venus between 529.65 and 529.85 $cm^{-1}$ (19 µm) recorded in 2021 and 2022. The signal-to-noise ratio in each spectrum is above 3000, so the error bars are not visible.

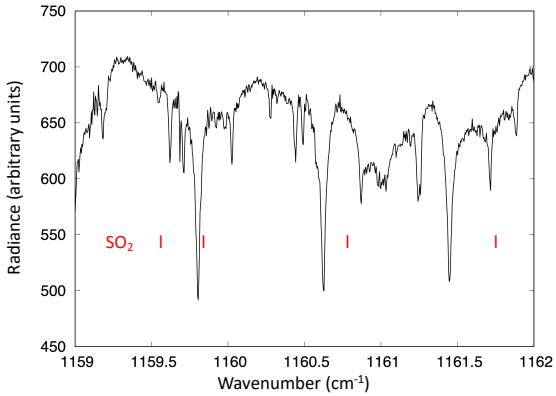


**Fig. 4.** Disk-integrated spectrum of Venus between 1159 and 1162 $cm^{-1}$ (8.6 µm) recorded on June 26, 2021. The positions of the strongest $SO_2$ lines ($S = 5 \times 10^{-21}$ $cm^{-2}$ $atm^{-1}$) are indicated. All the lines are due to terrestrial atmospheric absorption, in particular nitrous oxide and ozone.

very weak and unresolved; in addition, the curvature of the continuum induces some uncertainty in the $SO_2$ vmr retrieval, which translates into larger error bars than at 7.3 µm.

In addition to the 7.4 and. 19 µm spectral ranges, we devoted some observing time to the 8.6 µm (1160–1165 $cm^{-1}$) range,

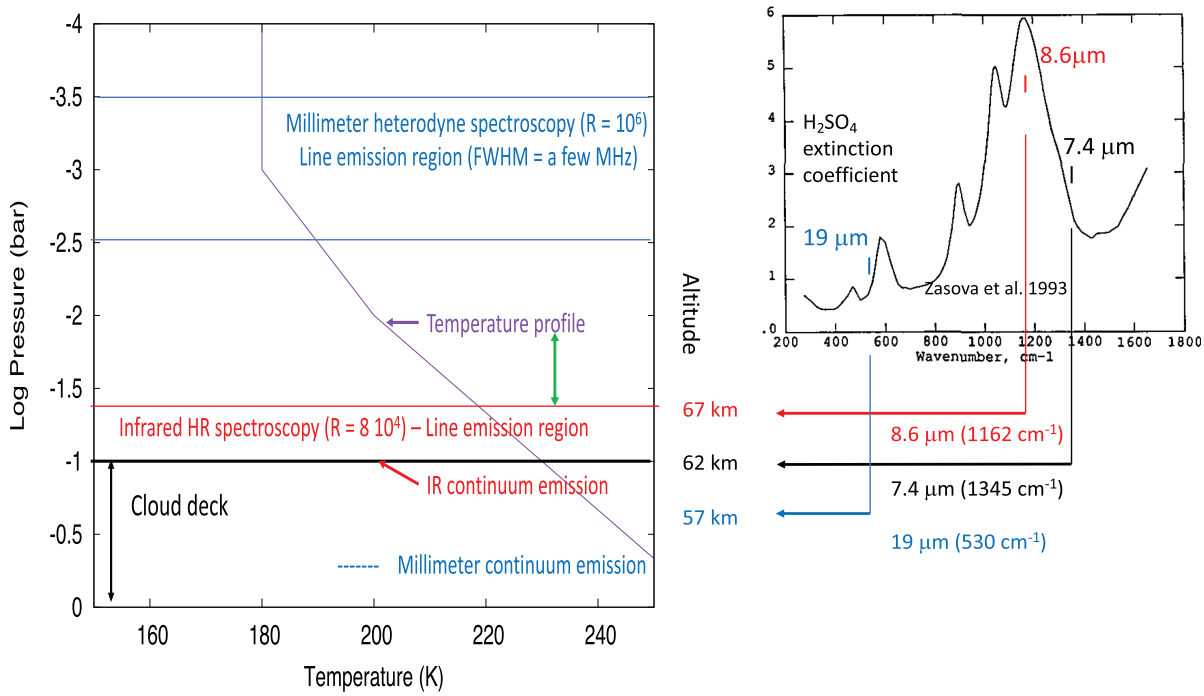


**Fig. 5.** Variations in the infrared penetration level as a function of the $H_2SO_4$ extinction coefficient. Left: penetration levels of the emitted infrared radiation at 8.6, 7.4, and 19 µm. Right: $H_2SO_4$ extension coefficient as a function of frequency, as shown by Zasova et al. (1993).

which also contains some transitions of the $\nu_1$ $SO_2$ band (Zasova et al. 1993). We searched for this band in February 2014 (E16), but failed to detect it. Its band strength is comparable to that of the $\upsilon_2$ band, but the penetration level at 1160 $cm^{-1}$ is a few kilometers above the cloud top (Zasova et al. 1993), where the $SO_2$ abundance is known to be depleted (E13). We searched again for $SO_2$ around 1162 $cm^{-1}$ in 2021 and 2022 without success; the $SO_2$ abundance has been especially low since 2021, as we discuss below. Figure 4 shows an example of the spectra recorded in this spectral range in 2021.

Figure 5 illustrates the three atmospheric levels probed in the different spectral ranges. At 1345 $cm^{-1}$ (7.4 µm), the cloud top is probed at a pressure level of about 100 mbar and a temperature of 230 K. At 530 $cm^{-1}$ (19 µm), the radiation comes from a few kilometers lower, at a pressure level of 250 mbar and a temperature of 241 K (E13). The altitudes of these levels are model-dependent since we have no information about the atmosphere below the penetration level. In addition, the pressure of the penetration levels was found to vary between the different runs recorded before 2020, corresponding to a change of a few kilometers in the altitudes of the penetration levels at 7.3 and 19 µm. Based on our previous studies, in the present paper we estimate the cloud top altitude at 62 km ($P$ = 100 mbar, $T$ = 230 K) and the 19 µm penetration level at 57 km ($P$ = 250 mbar, $T$ = 241 K). These values are taken as representative of the Venusian atmosphere, but may vary from run to run, as well as the temperature profile itself. At 1162 $cm^{-1}$ (8.6 µm), as mentioned above, the radiation comes from higher levels, a few kilometers above the cloud top; in our model, this level is situated at an altitude of around 67 km. As shown by Zasova et al. (1993), the altitude variations in the penetration levels at 8.6, 7.3 and 19 µm are due to the variations in the $H_2SO_4$ extinction coefficient, which is minimum at 19 µm and maximum at 8.6 µm (Fig. 5). By observing quasi-simultaneously the three spectral ranges, we can thus get a tridimensional image of the temperature field,

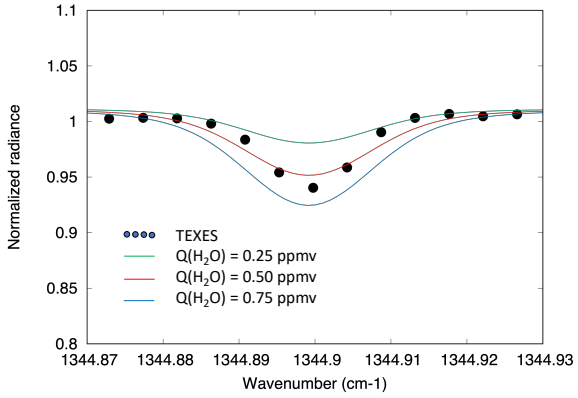


**Fig. 6.** Disk-integrated spectrum of the HDO transition at 1344.9 $cm^{-1}$ on Venus, recorded by TEXES on September 27, 2021 (black points). The continuum slope has been corrected to remove the telluric absorption (see Fig. 2). Models: $H_2O$ = 0.25 ppmv (green), 0.50 ppmv (red), and 0.75 ppmv (blue). The $H_2O$ vmr is inferred from the HDO vmr assuming a D/H ratio of 200 times the VSMOW. We infer from these fits a $H_2O$ vmr of 0.50 ± 0.25 ppmv. The $H_2O$ vmr inferred from the line depth ratio (see text) is 0.54 ± 0.20 ppmv.

and also retrieve information on the $SO_2$ vertical distribution (see Sect. 7).

Figures 6–8 show examples of spectral fits of the HDO line at 7.3 µm, and the $SO_2$ multiplets at 7.3 µm and 19 µm. We used the data of September 27, 2021 (maps 1345a and 530a), for which the $SO_2$ abundance was relatively high. To convert the HDO vmr into the $H_2O$ vmr, we assume, above the clouds, a D/H ratio of 200 times the Vienna Standard Ocean Water (VSMOW). We adopted this value in 2012, following Krasnopolsky (2010), as an averaged value from previous measurements (Bjoraker et al. 1992; Bertaux et al. 2007; Fedorova et al. 2008). We are aware of the uncertainty associated with this parameter

**Table 5.** Summary of TEXES observations obtained in 2021–2022 in the 1345 $cm^{-1}$ range and used for the analysis of the $SO_2$ plumes.

| Date of obs. | SEP E. long. | SSP E. long. | SEP LT (h) | Max $SO_2$ LT (h) | Min $SO_2$ LT (h) | Max $SO_2$ Latitude | Min $SO_2$ Latitude | $SO_{2max}$ (ppbv) | $SO_{2mean}$ (ppbv) |
|---|---|---|---|---|---|---|---|---|---|
| 2021/06/26 (b) | 239.1 | 274.2 | 14.3 | 20.0 | 19.0 | 30N | 0 | 300 | 160 |
| 2021/09/26 (a) | 124.1 | 197.7 | 16.9 | 18.0 | 17.0 | 0 | 10S | 420 | 123 |
| 2021/09/27 (b) | 126.7 | 200.8 | 16.9 | 18.0 | 17.5 | 10N | 0 | 360 | 135 |
| 2021/09/28 (b) | 129.3 | 203.9 | 17.0 | 17.5 | 16.5 | 10N | 10S | 390 | 141 |
| 2021/09/29 (b) | 131.9 | 206.9 | 17.0 | 22.0 | 21.5 | 10N | 0 | 330 | 100 |
| 2021/09/30 (a) | 134.5 | 210.0 | 17.0 | 13.0 | 10.5 | 0 | 15S | 360 | 140 |
| 2021/10/02 (a) | 139.7 | 216.1 | 17.1 | 13.5 | 10.0 | 15N | 10S | 330 | 86 |
| 2021/11/06 (b) | 228.1 | 323.4 | 18.4 | 19.0 | 17.0 | 40N | 30N | 270 | 57 |
| 2021/11/07 (b) | 230.6 | 326.5 | 18.4 | 14.0 | 13.0 | 20N | 20S | 300 | 58 |
| 2021/11/08 (a) | 233.0 | 329.6 | 18.4 | 20.0 | 14.5 | 20N | 20S | 420 | 120 |
| 2021/11/09/(a) | 235.4 | 332.6 | 18.5 | 24.0 | 22.5 | 20N | 15S | 420 | 77 |
| 2021/11/10 (a) | 237.8 | 335.7 | 18.5 | 24.0 | 22.5 | 30N | 15S | 270 | 53 |
| 2021/11/11 (a) | 240.2 | 338.6 | 18.6 | 14.0 | 13.0 | 20N | 15S | 420 | 88 |
| 2022/02/25 (a) | 54.3 | 306.9 | 4.8 | 6.0 | 4.0 | 0 | 30S | 180 | 90 |
| 2022/02/26 (b) | 56.6 | 310.1 | 4.9 | 6.0 | 5.0 | 25S | 30S | 180 | 92 |
| 2022/02/27 (a) | 58.8 | 313.1 | 5.0 | 7.0 | 4.5 | 0 | 20S | 180 | 108 |
| 2022/02/28 (b) | 61.5 | 316.2 | 5.0 | 6.0 | 5.0 | 25S | 30S | 180 | 107 |
| 2022/03/01 (a) | 63.4 | 319.3 | 5.1 | 6.0 | 4.0 | 30S | 35S | 180 | 97 |
| 2022/03/02 (b) | 65.7 | 322.4 | 5.1 | 5.5 | 4.5 | 25S | 30S | 180 | 100 |
| 2022/03/03 (b) | 68.0 | 325.5 | 5.2 | 6.0 | 3.0 | 30N | 0 | 240 | 115 |
| 2022/06/25 (a) | 4.0 | 317.0 | 8.9 | 5.0 | 3.5 | 20N | 10N | 200 | 140 |
| 2022/06/26 (b) | 6.8 | 321.1 | 9.0 | 5.0 | 3.5 | 15N | 0 | 240 | 174 |
| 2022/06/27 (a) | 9.3 | 324.0 | 9.0 | 14.0 | 13.0 | 0 | 15S | 240 | 132 |
| 2022/06/29 (c) | 15.0 | 330.5 | 9.0 | 7.0 | 5.0 | 0 | 15S | 200 | 96 |
| 2022/06/30 (b) | 17.4 | 333.3 | 9.1 | 7.5 | 6.5 | 10N | 10S | 270 | 174 |
| 2022/07/01 (b) | 20.1 | 336.4 | 9.1 | 14.0 | 13.0 | 10N | 10S | 390 | 138 |
| 2022/07/03 (a) | 25.4 | 342.4 | 9.1 | 8.0 | 7.0 | 20N | 10S | 200 | 120 |
| 2022/07/04 (a) | 28.1 | 345.6 | 9.2 | 7.0 | 5.0 | 15N | 10S | 270 | 174 |

**Notes.** Times refer to the beginning of the observations. SEP and SSP refer to the sub-Earth point and the sub-solar point, respectively. Max $SO_2$ LT and Min $SO_2$ LT define the local time interval where the $SO_2$ plume appears. Max $SO_2$ Latitude and Min $SO_2$ Latitude define the latitude interval in which the $SO_2$ plume appears. $SO_{2max}$ indicates the $SO_2$ vmr observed inside the interval where $SO_2$ is maximum. $SO_{2mean}$ is the mean $SO_2$ vmr over the disk, derived from the disk-integrated spectrum at 1345 $cm^{-1}$.

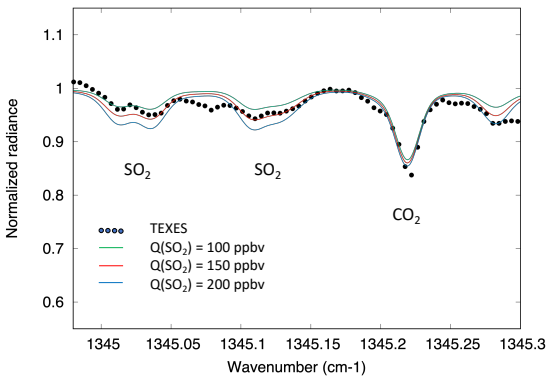


**Fig. 7.** Disk-integrated spectrum of Venus between 1344.95 and 1345.30 $cm^{-1}$ recorded by TEXES on September 27, 2021 (black points). A weak telluric absorption appears between the two $SO_2$ multiplets. Models: $SO_2$ = 100 ppbv (green), 150 ppbv (red), and 200 ppbv (blue). We infer from these fits a $SO_2$ vmr of 125 ± 25 ppbv. The $SO_2$ vmr inferred from the line depth ratio (see text) is 135 ± 14 ppbv.

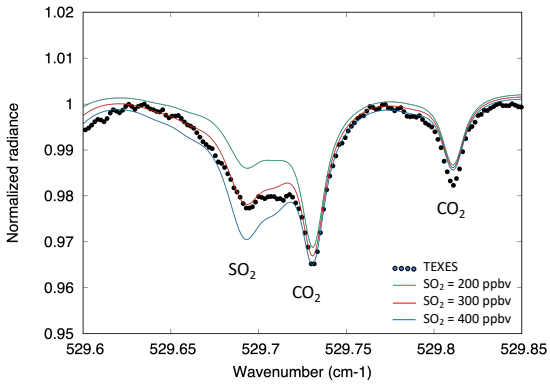


**Fig. 8.** Disk-integrated spectrum of Venus between 529.6 and 529.85 $cm^{-1}$ recorded by TEXES on September 27, 2021 (black points). Models: $SO_2$ = 200 ppbv (green), 300 ppbv (red), and 400 ppbv (blue). We infer from these fits a $SO_2$ vmr of 325 ± 25 ppbv. The $SO_2$ vmr inferred from the line depth ratio (see text) is 350 ± 75 ppbv.

(Krasnopolsky et al. 2013), but we keep the enrichment factor of 200 with respect to the terrestrial value for consistency within our analysis. As in our previous studies, the synthetic spectra were calculated using a line-by-line radiative transfer code without scattering (E12, E13, E16). Our thermal profile was inferred from the inversion of the TEXES data in the strong

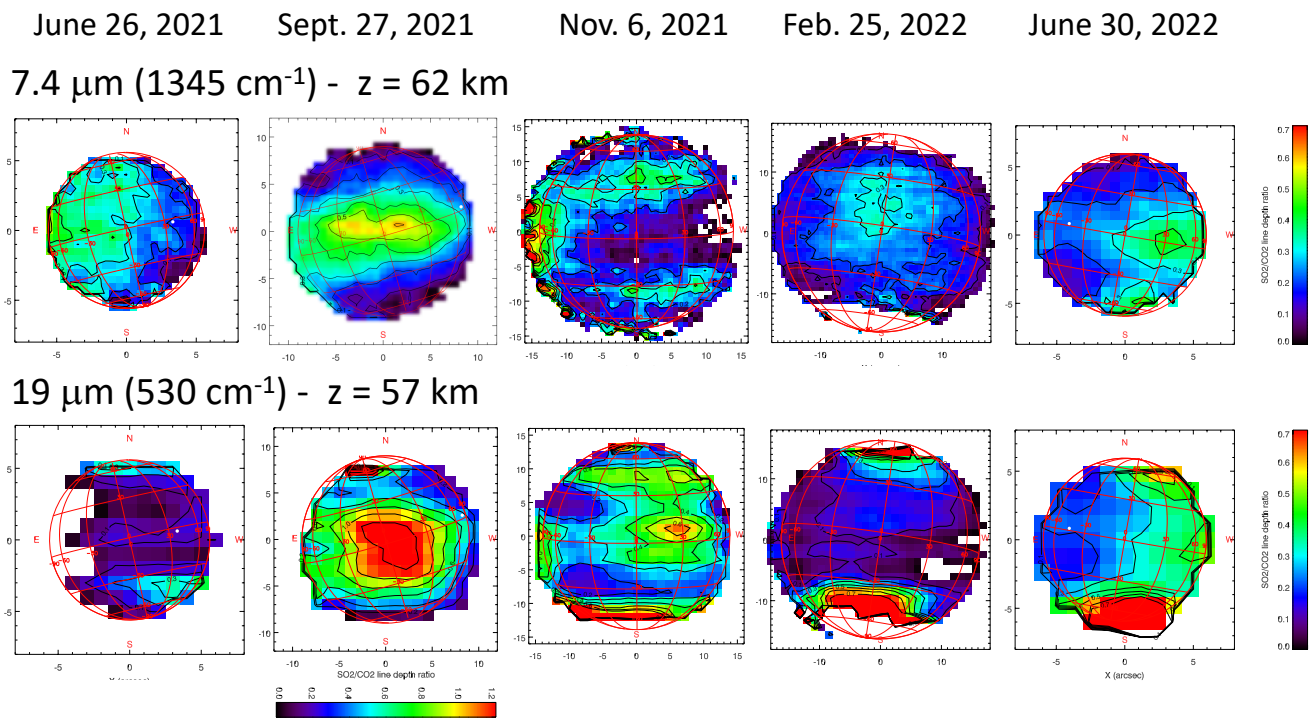


**Fig. 9.** Examples of $SO_2$ maps recorded in 2021–2022. Top: maps of the line depth ratio of a weak $SO_2$ multiplet (around 1345.1 $cm^{-1}$) to the $CO_2$ transition at 1345.22 $cm^{-1}$, recorded in 2021 and 2022 (one map per observing run). Disk-integrated spectra corresponding to these maps are shown in Fig 2. Bottom: maps of the line depth ratio of a weak $SO_2$ multiplet (around 529.70 $cm^{-1}$) to the $CO_2$ transition at 529.81 $cm^{-1}$, recorded in 2021 and 2022 (one map per observing run). For the 19 μm maps, the maximum scale is 0.7, except for September 2021 for which the maximum scale is 1.2, as indicated below the map. Disk-integrated spectra corresponding to these maps are shown in Fig. 3. The local maxima observed in 2022 near the south pole (bottom right) are instrumental artifacts, due to the nearly isothermal profile at high latitude, which prevents the $SO_2$ retrieval.

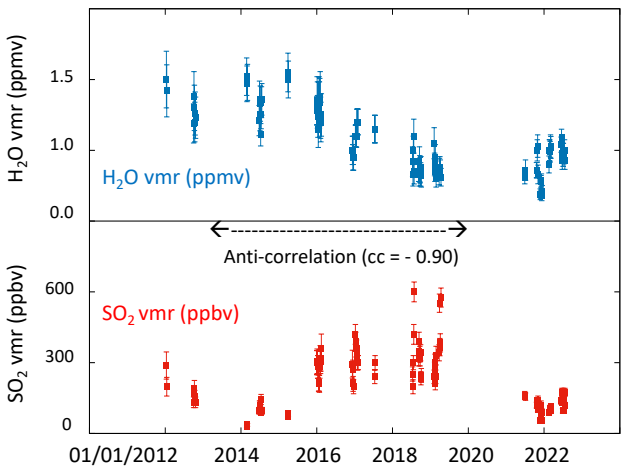


**Fig. 10.** Comparative long-term temporal evolution of $H_2O$ and $SO_2$ at the Venus cloud top. Top: long-term variations in the $H_2O$ vmr (blue points), inferred from the HDO measurements at the cloud top from the TEXES data at 7.4 μm. Bottom: long-term variations in the $SO_2$ vmr inferred at the cloud top (7.4 μm, red points). A daily value is shown in this figure.

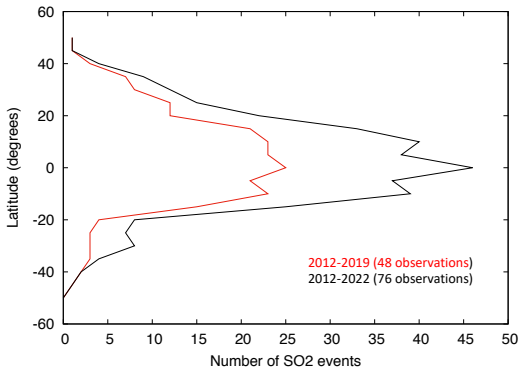


**Fig. 11.** Distribution of the location of the $SO_2$ plumes as a function of latitude (black line). The total number of observations is 76. Red line: distribution obtained without the 2021–2022 data (48 observations, Fig. 12 in E20).

11101–10002 $CO_2$ Q-branch absorption feature at 791.4 $cm^{-1}$ (12.6 μm) recorded shortly after our observations (Giles et al. 2022). As in our previous studies (E13, E16), a cutoff was introduced in the $SO_2$ vertical distribution, five kilometers above the cloud top. This cutoff is needed to fit the $SO_2$ lines, which are broader than the $CO_2$ lines (E13, E16).

Figure 9 shows examples of maps of the $SO_2$ vmr obtained at 7.4 and 19 μm, from the data shown in Figs. 2 and 3, using the transitions mentioned above. For each run, one map is shown. As in our previous studies, we derived the HDO and $SO_2$ mixing ratios from the ldr of weak HDO and $SO_2$ lines divided by a weak nearby $CO_2$ line (E12, E16). For the conversion from ldr into vmr, the following equations, based on previous spectral fits (E12, E13, E16), are used:

– At 7.4 μm (1345 $cm^{-1}$), vmr($SO_2$)(ppbv) = ldr($SO_2$) × 600.0; vmr($H_2O$)(ppmv) = ldr (HDO) × 1.5.

– At 19 μm (530 $cm^{-1}$), vmr($SO_2$)(ppbv) = ldr($SO_2$) × 500.0.

In the case of HDO, we infer from the fits (Fig. 6) a $H_2O$ vmr of 0.50 ± 0.25 ppmv, while the $H_2O$ vmr retrieved from the ldr (shown in Fig. 10) is 0.54 ± 0.20 ppmv. In the case of $SO_2$,

we infer from the fits at 7.4 µm (Fig. 7) a $SO_2$ vmr of 125 ± 25 ppbv, while the $SO_2$ vmr derived from the ldr is 135 ± 14 ppbv (Table 5 and Fig. 10); at 19 µm (Fig. 8), we infer from the fits a $SO_2$ vmr of 325 ± 25 ppbv, while the $SO_2$ vmr retrieved from the ldr is 350 ± 75 ppbv (Fig. 19). The mixing ratios calculated from the equations mentioned above are thus in good agreement with the values inferred from the spectral fits. As in our previous studies, the HDO maps inferred from the 7.4-µm spectra (Fig. 2) are homogeneous over the disk.

## 3. Long-term variations in $SO_2$ and $H_2O$

Figure 10 shows the temporal variations in the $H_2O$ and $SO_2$ mixing ratios derived from the 7.4 µm data. These mixing ratios refer to the cloud top located, in our model, at an altitude of z = 62 km.

The first comment to be made is that the $SO_2$ abundance at the cloud top significantly decreased after 2020, compared to the high values reached in 2018 and 2019. In parallel, the water abundance remained more or less constant, at a rather low level, compared to the high values reached in 2012–2016. In our previous analysis (E20), we reported a clear anti-correlation of the two molecules (cc = –0.9) between 2014 and 2019. This anti-correlation is no longer visible in 2021–2022, nor was it present in 2012–2014. Possible reasons for this behavior are discussed in Sect. 7. The relative time variations in $SO_2$ at 7.4 and 19 µm are discussed below (see Sect. 6).

## 4. A statistical study of the $SO_2$ plumes

This analysis is performed using the $SO_2$ maps at the cloud top, obtained from the 7.4 µm data. Using the whole TEXES dataset since 2012, we extended our statistical study of the $SO_2$ plumes (E19, E20) with respect to their distribution as a function of latitude, longitude, and local time (LT). Our method, fully described in earlier papers (E19, E20), consists in selecting one map per day (the one showing the $SO_2$ plume with the strongest vmr) and evaluating, on each map, the latitude, longitude, and LT range of the plume. In the case of the latitude distribution, we simply sum up, at each latitude, the maps for which the plume is present (Fig. 11). In the case of the longitude or LT distribution, our method is the following. We evaluate, from each map, the longitude or the LT range over which the $SO_2$ plume is present, assigning a probability of 1 within this range, and 0 outside this range. In parallel, we assign a probability of 1 over the whole observed longitude or LT range (180 degrees or 12 h corresponding to the observed hemisphere of the planet). Then, for each longitude or LT, we sum up all maps for which this longitude or LT is observed, and, separately, all maps for which a $SO_2$ plume is present at the given longitude or LT. Dividing the latter curve by the former gives us the probability for a $SO_2$ plume to be present at a given longitude (Fig. 12) or LT (Fig. 13).

Table 5 lists the new data from the 2021 and 2022 runs, which complement the previous dataset shown in Table 1 of E20. This table gives, in sequence for each observation, the longitude of the sub-Earth point (SEP), the longitude of the sub-solar point (SSP), the LT of the SEP, the LT range of the observed $SO_2$ plume (where the probability is 1), the latitude range of the $SO_2$ plume, the maximum $SO_2$ vmr within this plume (measured from the $SO_2$ map), and the mean $SO_2$ vmr (derived from the disk-integrated spectrum). The last two quantities are not used when we calculate the probability of $SO_2$ plume appearance, but are used in the next step (Sect. 5).

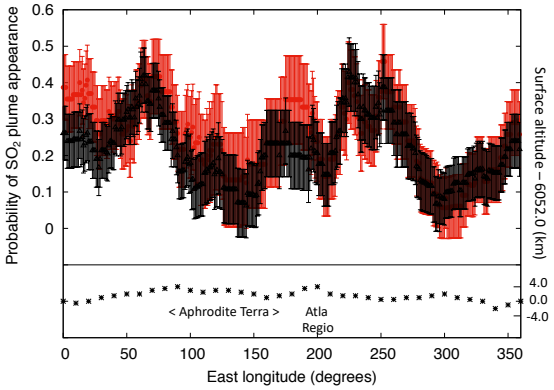


**Fig. 12.** Longitudinal distribution of the $SO_2$ plumes. Top: probability of $SO_2$ appearance as a function of longitude using the whole dataset (2012–2022, black points). The total number of observations is 76. The error bar is proportional to $n^{-0.5}$, where $n$ is the number of observations for which the longitude is observed. Red points: dataset without the 2020–2021 data (Fig. 19 of E20). Bottom: surface altitude of Venus in the equatorial region as a function of longitude.

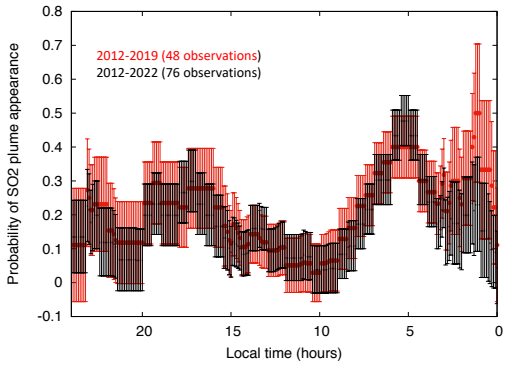


**Fig. 13.** Probability of $SO_2$ appearance as a function of local time, using the whole 2012–2022 dataset (black points). The error bar is proportional to $n^{-0.5}$, where $n$ is the number of observations for which the local time is observed. Red points: dataset without the 2020–2021 data, as shown in Fig. 14 of E20. The local hour scale increases from right to left, corresponding to the orientation on the Venus disk as seen by an external observer.

### 4.1. Distribution of the $SO_2$ plumes as a function of latitude

Figure 11 (an update of Fig. 12; E20) shows the distribution of the $SO_2$ plumes as a function of latitude. This figure confirms our earlier result (E19; E20) indicating a strong peak around the equator. We recall that we have no information for latitudes higher than 60 degrees north and south, due to the peculiar shape of the thermal profile around the polar collar, especially when the morning terminator is observed; in this case, when the thermal profile becomes close to isothermal, the retrieval of $SO_2$ and HDO is no longer possible. For this reason, we limit our statistical analysis of the $SO_2$ plumes within 50 degrees of the equator.

### 4.2. Distribution of the $SO_2$ plumes as a function of longitude

We completed our analysis of the $SO_2$ plume distribution as a function of longitude, using the same method as described in E19 and using the 76 data points available (Table 1 of E19 and Table 5 of this paper). The results are shown in Fig. 12. As done previously (E19; E20), we added all observable longitude ranges

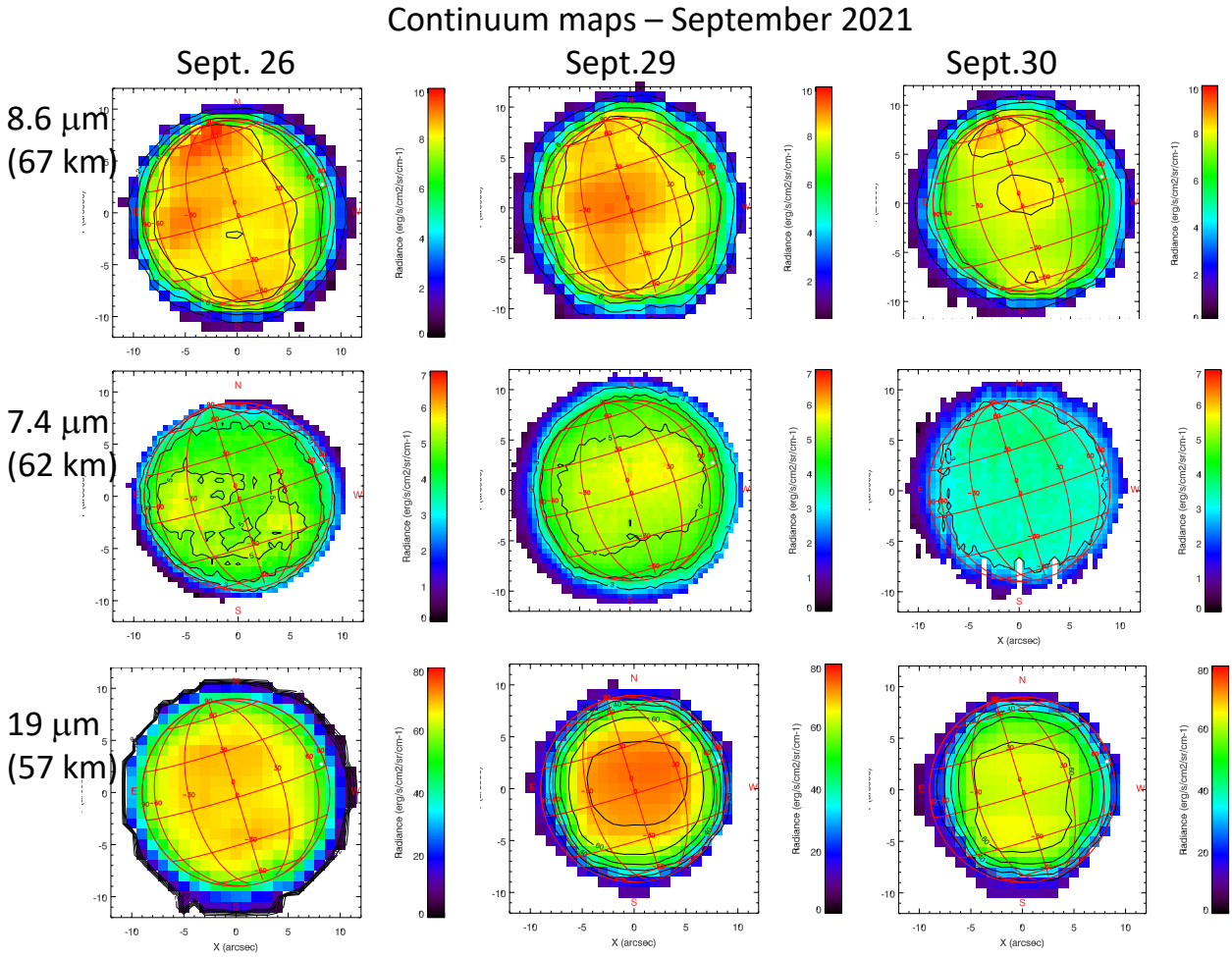


**Fig. 14.** Continuum maps recorded during the September 2021 run at 8.6 µm (top), 7.4 µm (middle), and 19 µm (bottom). The three spectral ranges probe altitude levels of 67, 62, and 57 km, respectively.

to obtain the longitude visibility curve corresponding to our dataset; in the same way, we added all longitude ranges where a $SO_2$ plume was present. Dividing this curve by the longitude visibility curve gives us the probability of $SO_2$ appearance as a function of the longitude (Fig. 12). As in our previous study, there is no clear trend in the longitudinal distribution of the probability of $SO_2$ plume appearance, except possible local maxima around 60 E and 225 E, which show no clear correlation with the topography around the equator (Fig. 12).

### *4.3. Distribution of the $SO_2$ plumes as a function of local time*

In this section, we estimate the probability of $SO_2$ plume appearance as a function of local time, using the method described above and the whole dataset of 76 points (2012–2022). Figure 13 shows the probability of $SO_2$ plume appearance as a function of local time. A depletion appears around 10:00, with a clear enhancement around the terminators, confirming our earlier results. The comparison with the earlier results (Fig. 14; E20) shows that as the error bars decrease with the increasing number of observations, the new curve is consistent with the previous ones, which gives us confidence in the result.

As mentioned earlier, the analysis described above considers only the location of the $SO_2$ plumes as a function of local time, and not their intensity; its main advantage is that it separates the study of the probability of $SO_2$ appearance as a function of longitude (or local time) from the study of the long-term temporal variations in $SO_2$, since all observations have the same weight, whatever the disk-integrated $SO_2$ vmr is. The limitation of this analysis, however, is that it does not allow us to compare our results with those of other instruments using occultation techniques like SPICAV/Venus Express, which do not have the capability of mapping the planet instantaneously. For this reason, in our last analysis (E20), we estimated the $SO_2$ vmr as a function of longitude (Fig. 21; E20) and local time (Fig. 16; E20). We repeated this exercise using the whole dataset (2012–2022), both for the longitude and the local time $SO_2$ vmr distributions, but the results were found to be inconclusive, with the new plots being outside the error bars of the previous ones. The reason is probably that the $SO_2$ vmr was significantly lower in the 2021–2022 data, which corresponded to only a fraction of the longitude/LT range; as a result the temporal variability of $SO_2$ could not be disentangled from the longitude and the LT. We thus excluded this analysis from the present paper.

## 5. Unusual behavior of $SO_2$ plumes in September–November 2021

In September and November 2021 we first noticed an unusual behavior of the continuum maps. As shown in earlier papers,

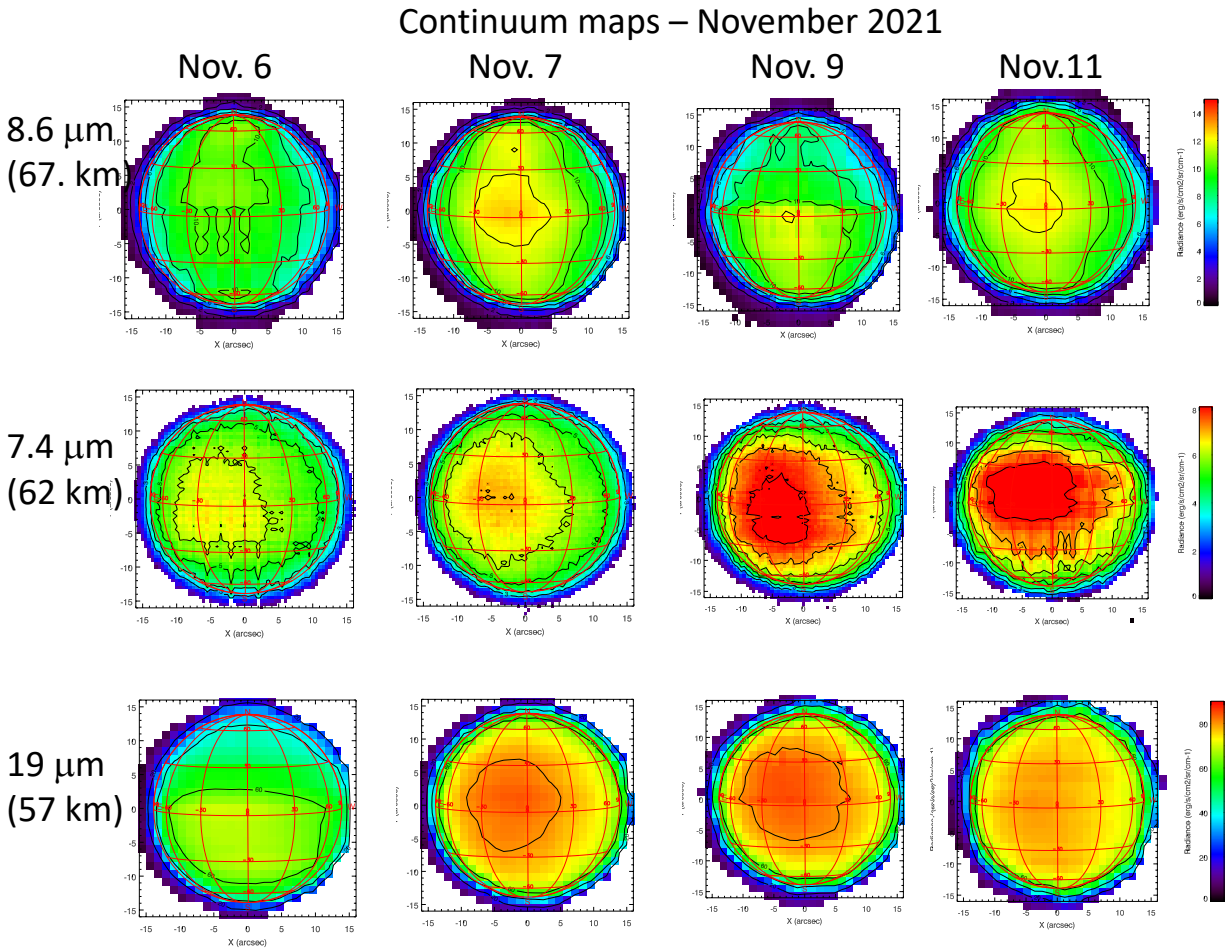


**Fig. 15.** Continuum maps recorded during the November 21 run at 8.6 μm (top), 7.4 μm (middle), and 19 μm. (bottom) The three spectral ranges probe altitude levels at 67, 62, and 57 km, respectively.

these continuum maps, which give the temperature distribution at different atmospheric levels, are usually globally symmetrical around the disk center where the radiation is maximum (E13, E16).

Figures 14 and 15 show the continuum maps recorded in the three spectral ranges in September and November 2021. It can be seen on September 26, 29, and 30 that the 8.6 μm maps ($z$ = 67 km) show an unusual feature with a polar and equatorial enhancement; on September 26 the equatorial enhancement is above the evening terminator. The same behavior is observed in the 8.6 μm maps of November 7 and 11 (Fig. 15). This behavior was not observed in any other run. In November 2021 we also observed a strong increase in the temperature at the cloud top on November 9, which started at lower levels on November 7 and lasted until November 11. In September and in November 2021 the flux contrast associated with these features was about 10% (Figs. 14 and 15), which corresponds to a 3 K contrast in brightness temperature at 8.6 μm.

In parallel, we observed a strong activity of the $SO_2$ plumes. On September 27 a strong plume is visible on the 19 μm $SO_2$ map, but disappears the next day (Fig. 16). In November (Fig. 17), a strong plume appears at 57 km on Nov. 7, develops and extends up to the cloud top on Nov. 8, and is still visible at both levels on November 9. It seems that the same plume is apparent over three days, as its location follows the four-day cloud rotation at the cloud top. If this interpretation is true, it implies that this strong plume has a lifetime of more than 48 h, which is exceptional. This is the first time that we have seen the same plume on three successive days.

The strong plume activity shown in September and November 2021 is surprising as this period corresponds to a low $SO_2$ abundance at the cloud top (Fig. 10). In order to better quantify the plume activity, we plotted the ratio of the maximum $SO_2$ vmr (measured on the $SO_2$ maps) to the mean $SO_2$ vmr (inferred from the disk-integrated spectrum) as a function of time. Both quantities are listed in the two right columns of Table 5. Figure 18 shows this ratio, compared with the $SO_2$ vmr at the cloud top as a function of time (same as in Fig. 10). Two comments can be made about this plot. First, the $[SO_{2max}]/[SO_{2mean}]$ ratio has been remarkably constant since 2012, with a mean value around 1.5–2.0. This tends to indicate that the $SO_2$ plume activity increases more or less linearly with the $SO_2$ abundance. Second, there is a noticeable exception in November 2021; at that time the ratio reaches values of 5–6. We note that this was not the case in February 2014, when the $SO_2$ abundance at the cloud top reached its absolute minimum value.

## 6. Long-term evolution of the $SO_2$ vertical distribution

In previous analyses (E13; E16) we tried to derive information about the vertical profile of $SO_2$ by studying simultaneously the $SO_2$ spectra obtained at 7.4 and 19 μm. Motivated by the

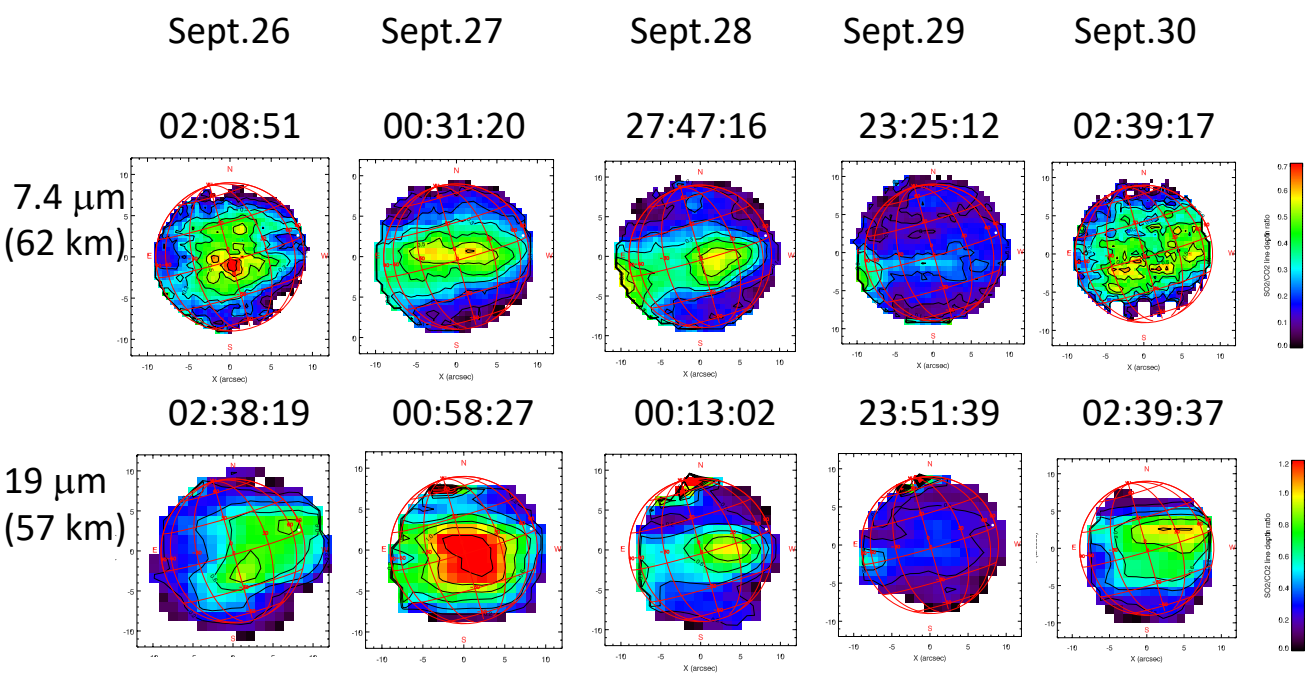


**Fig. 16.** Examples of $SO_2$ maps recorded in September 2021. Top: maps of the line depth ratio of a weak $SO_2$ multiplet (around 1345.1 $cm^{-1}$) to the $CO_2$ transition at 1345.22 $cm^{-1}$, recorded in September 26, 27, 28, 29, and 30, 2021. Bottom: maps of the line depth ratio of a weak $SO_2$ multiplet (around 529.69 $cm^{-1}$) to the $CO_2$ transition at 529.81 $cm^{-1}$, recorded on the same days. Times refer to the beginning of the observations. The maps of September 27 correspond to the spectra shown in Figs. 2, 3, and 6–8.

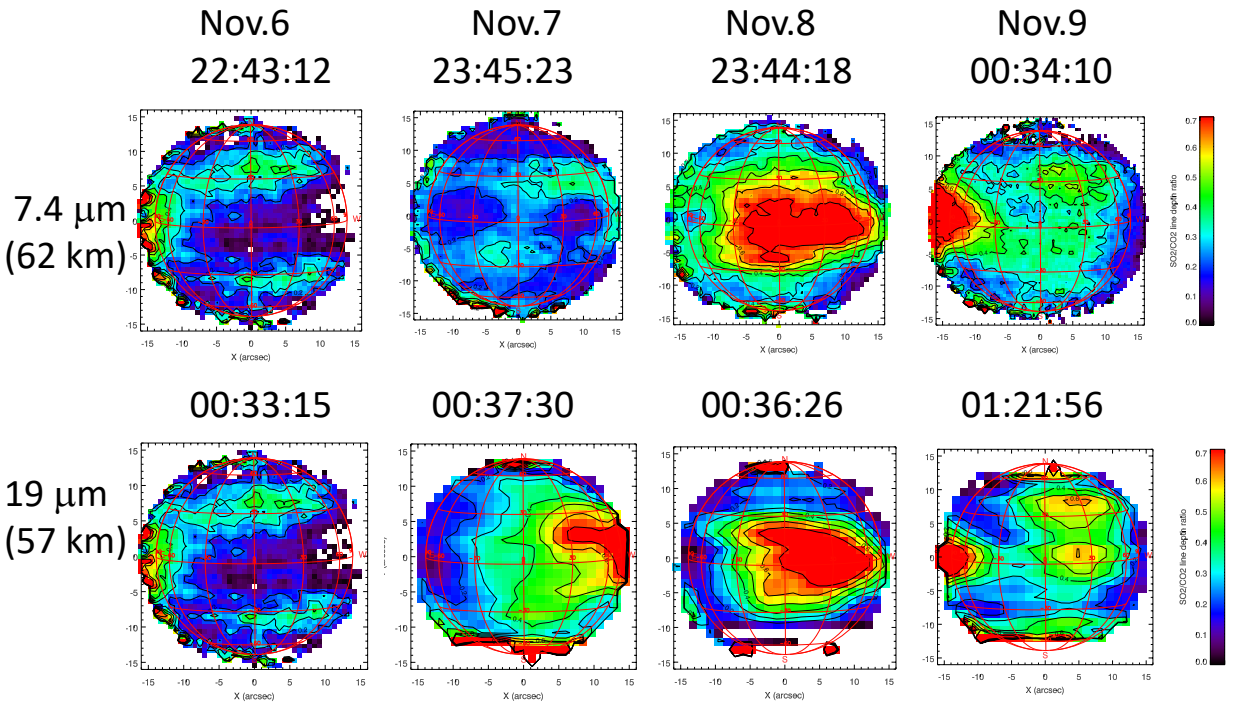


**Fig. 17.** Examples of $SO_2$ maps recorded in November 2021. Top: maps of the ldr of a weak $SO_2$ multiplet (around 1345.1 $cm^{-1}$) to the $CO_2$ transition at 1345.22 $cm^{-1}$, recorded in November 6, 7, 8, and 9, 2021. Bottom: maps of the line depth ratio of a weak $SO_2$ multiplet (around 529.69 $cm^{-1}$) to the $CO_2$ transition at 529.81 $cm^{-1}$, recorded on the same days. Times refer to the beginning of the observations.

anomalous behavior observed in November 2021, we extended this analysis over the whole dataset (2012–2022). Figure 19 shows the $SO_2$ mixing ratios as a function of time, both at 7.4 µm ($z$ = 62 km) and at 19 µm ($z$ = 57 km). It can be seen that, in most of the cases, the two quantities are comparable (with a ratio between 0.7 and 1.5), which implies that, in most of the cases, in the few kilometers below the cloud top the $SO_2$ mixing ratio is more or less constant. There are a few exceptions, however. The most noticeable one appears in November 2021; between the altitude levels of 57 km and 62 km, the $SO_2$ vmr decreases by a factor higher than 4. In February 2014 and December 2015, the $SO_2$ vmr decreases by a factor of about 2. Figure 19 shows another surprising behavior. In some cases the $SO_2$ vmr at 57 km is lower than that at 62 km. This is especially visible in June 2021

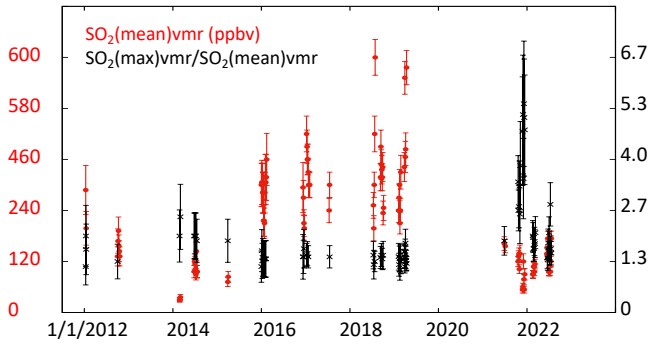


**Fig. 18.** $[SO_{2max}]/[SO_{2mean}]$ ratio as a function of time (black points); the two parameters are listed in Table 5. Red points: mean (disk-integrated) $SO_2$ vmr at the cloud top as a function of time; this plot is the same as in Fig. 10.

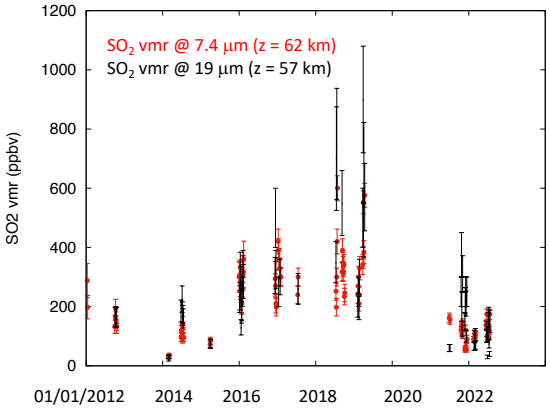


**Fig. 19.** Mean (disk-integrated) $SO_2$ vmr at 57 km, inferred from the 19 µm data, as a function of time (black points); red points: mean (disk-integrated) $SO_2$ vmr at the cloud top (62 km), inferred from the 7.4 µm data, as a function of time.

and June 22 when the $[SO_2(57\,km)/SO_2(62\,km)]$ ratio is lower than 0.5. We have no explanation for these temporal variations.

In September 2018, the $SO_2$ mixing ratio at the cloud top is at its maximum; the plume activity is strong, but not exceptional; in November 2021, the $SO_2$ mixing ratio is very low, but the plume activity is strong. Figure 20 shows the comparative evolution with time of the $SO_2$ abundance, the $SO_2$ plume contrast, and the $SO_2$ vertical gradient.

Regarding the $SO_2$ vertical distribution above the cloud top, we know that $SO_2$ decreases abruptly within a few kilometers, as indicated by the shape of the $SO_2$ lines (E13); this is why we have not yet been able to detect $SO_2$ at 8.6 µm. However, at the time of our observations (in February 2014 and since 2021), the $SO_2$ abundance has always been very low. This observation will have to be repeated in the future as it could provide a constraint on the $SO_2$ vertical gradient above the cloud top if the $SO_2$ abundance increases again.

## 7. Discussion and conclusions

In this paper, we pursued our $SO_2$ and HDO monitoring at the cloud top of Venus using the TEXES instrument at 7.4 µm by adding new data obtained in 2021 and 2022, and completing the $SO_2$ analysis at 19 µm. We also considered the 8.6 µm data which give information on the temperature field a few kilometers above the cloud top. We reanalyzed the whole TEXES dataset between 2012 and 2019 to study the long-term behavior of $H_2O$

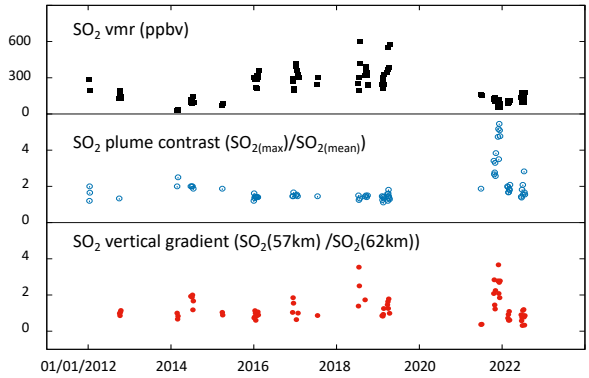


**Fig. 20.** Evolution of the $SO_2$ abundance atop and within the Venus cloud between 2012 and 2022, as observed by TEXES. Top: mean (disk-integrated) $SO_2$ vmr at the cloud top (62 km), inferred from the 7.4 µm data, as a function of time (same as in Fig. 10). Middle: $[SO_{2max}]/[SO_{2mean}]$ ratio as a function of time (same as Fig. 18). Bottom: $[SO_2(57\,km)/SO_2(62\,km)]$ ratio as a function of time.

and $SO_2$, and the behavior of $SO_2$ as a function of latitude, local time, and longitude. The main results of this study can be summarized as follows.

(1) After 2020, the $SO_2$ abundance at the cloud top decreased by a factor of about 3 with respect to its maximum 2018 value, and remained at this low value between June 2021 and July 2022, while the $H_2O$ abundance was comparable to its 2018–2019 value (Fig. 10).

(2) The anti-correlation between $H_2O$ and $SO_2$, which was observed between 2014 and 2019, is no longer visible. We wonder whether this lack of anti-correlation could be linked to the strong $SO_2$ plume activity, which might mix the different minor species in an upward convective ascending motion. However, the lack of anti-correlation is observed in all runs since 2020, and not only in November 2021, so this explanation is not sufficient.

The cause of the anti-correlation of $SO_2$ and $H_2O$ at the cloud top observed by TEXES was investigated through a one-dimensional photochemical model by Shao et al. (2020). This study found that the anti-correlation could be attributed to the sulfur chemistry, while the vertical mixing tends to make the two species positively correlated. From this perspective, the decrease in the anti-correlation might be related to the increase in the vertical mixing in the clouds. The vertical mixing in the clouds is very probably not constant over time. Marcq et al. (2013) discussed the possibility of the intrinsic dynamical variability in the global circulation causing the long-term variation in $SO_2$ at 70 km. Lefèvre et al. (2022) use a three-dimensional convection-resolving dynamical model to obtain the vertical mixing in the cloud layer. The Venus Monitoring Camera (VMC) observed the cellular features at cloud top altitudes, at the sub-solar point suggesting convective activity (Markiewicz et al. 2007; Titov et al. 2012). Lefèvre et al. (2018) with the IPSL Venus mesoscale model resolved convective activity at this altitude range, linked with the strong solar absorption of the unknown UV absorber. However, the different radio occultation on board the Venus Express and the Akatsuki radio occultation did not measure any convective layer at the sub-solar point at cloud-top (Ando et al. 2018, 2020). The observed long-term variations in Venus' 365 nm albedo (Lee et al. 2019) would have a strong effect on the intensity on such cloud convective activity. However, it is still not well understood how the vertical mixing or dynamics in the clouds varies with time and affects the behaviors of $SO_2$

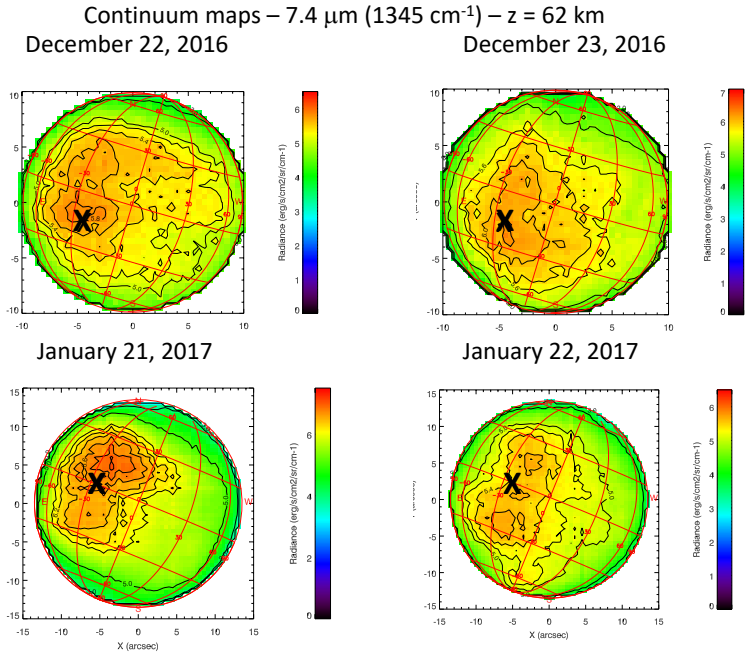


**Fig. 21.** Examples of continuum maps indicating the possible presence of mountain waves. Top: continuum maps recorded at 1345 $cm^{-1}$, probing the cloud top (62 km), on December 22 (left) and December 23 (right), 2016. On December 22, 2016, the SEP longitude was 157.3 E and the evening terminator longitude was 144.7 E. The black crosses indicate the position of Thetis Regio. Bottom: continuum maps recorded at 1345 $cm^{-1}$, probing the cloud top (62 km), on January 21 (left) and January 22 (right), 2017. On January 21, 2017, the SEP longitude was 233.1 E and the evening terminator longitude was 237.4 E. The black crosses indicate the position of Atla Regio.

and $H_2O$ at the cloud top. As well as atmospheric dynamics, external forces like volcanism (e.g., Esposito 1984), cosmic rays, and solar activity (Lee et al. 2019) may also cause the variations in chemical species at the cloud top. However, these possible mechanisms are also not well understood, due to the lack of continuous observations and a comprehensive atmospheric model.

(3) The new analysis of the probability of $SO_2$ plume occurrence as a function of local time confirms our previous results (E19; E20) with a maximum around the equator (Fig. 11), as expected from dynamical models, and two maxima around the terminators, especially around 06:00 LT (Fig. 13). As in our previous analysis, the probability of $SO_2$ plume occurrence as a function of longitude shows no clear feature, except a possible maximum around 60 E and 225 E (Fig. 12); however, this distribution in longitude does not correspond to any topographic feature and its significance remains to be confirmed.

(4) An analysis of the thermal maps at 8.6, 7.4, and 19 μm shows some unusual features in September and November 2021, with, in some cases, the apparition of polar and equatorial localized enhancements. We wonder whether these anomalies might be linked to large-scale gravity waves, such as the mountain waves previously observed by Akatsuki (Fukuhara et al. 2017; Kouyama et al. 2017). Between 2015 and 2017, large-scale stationary gravity waves were observed by the Longwave Infrared Camera (LIR) of the Akatsuki spacecraft. The temperature contrast associated with these waves was as high as 3 K. These features were preferentially observed over high-altitude areas, generated by the mountain waves forcing the flow to go above them, but they also appeared preferentially around the evening terminator, where the near-surface atmosphere is more stable and suitable for the propagation of the waves (Lefèvre et al. 2020).

In September and November 2021, the evening terminator was observed. The continuum maps at 8.6 μm on September 26

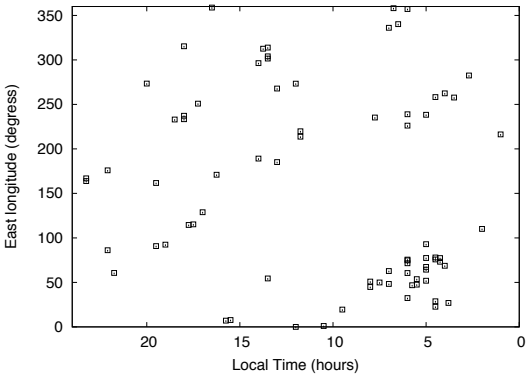


**Fig. 22.** Location of the $SO_2$ plumes used in our statistical analysis (Sect. 4), plotted as a function of their local time and their east longitude. These locations do not appear to be associated with mountain waves. The different points of a given run are aligned along a straight line of slope +15 degrees $h^{-1}$, reflecting the relationship between LT and the longitude for this given run.

(Fig. 14) and on November 7 (Fig. 15) distinctly show a wave above the evening terminator, as observed on several occasions by the LIR camera aboard Akatsuki; in addition, the temperature amplitude of the wave observed by TEXES is in the range of 3 K, in agreement with the results of Akatsuki (Kouyama et al. 2017). These analogies suggest that the same kind of wave is observed with TEXES. The region observed by TEXES in September 2021 is above Aphrodite Terra; however, the one observed in November 2021 is east of Maats Mons by about 30 degrees, so more investigation is needed to assess the nature and the origin of the phenomenon.

We have been looking at the TEXES database to search for other possible anomalous features in the thermal maps.

We found two specific cases in the 7.3 µm continuum maps, on December 22 and 23, 2016, and on January 21 and 22, 2017 (Fig. 21). In both cases the evening terminator was observed. A meridional double structure appears, not far from this terminator. In December 2016, the feature is located above Thetis Regio (above 4 km high), while in January 2017 it is above Atla Regio (up to 4 km high). These features might be another example of mountain waves.

Finally, we wonder if the occurrence of the $SO_2$ plumes could be also associated with gravity waves. To test this hypothesis, we plotted the 76 $SO_2$ plumes used in our analysis (Sect. 4) as a function of their local hours and their longitudes, taken as the central values of the intervals used in our analysis (Fig. 22). If the $SO_2$ plume occurrence were associated with mountain waves, we would expect an accumulation of points around 18:00 and above the mountains. However, this is not the case: a cluster of points appears around 50 E longitude (which is consistent with Fig. 12) and around 6:00 LT (as expected from Fig. 13). Thus, we see no connection between the $SO_2$ plume appearance and the mountain waves tentatively detected in our thermal maps.

(5) An anomalous behavior of the $SO_2$ plumes is also observed in November 2021, associated with a very strong plume activity and a strong $SO_2$ gradient in the few kilometers below the cloud top. For the first time we see a plume with a lifetime that might exceed 48 h. In the future more monitoring of the planet in the three spectral ranges analyzed in this paper will be needed to better understand the dynamical evolution of $SO_2$ below and above the cloud top.

*Acknowledgements.* T.E., T.K.G. and R.G. were visiting astronomers at the NASA Infrared Telescope Facility, which is operated by the University of Hawaii under Cooperative Agreement no. NNX-08AE38A with the National Aeronautics and Space Administration, Science Mission Directorate, Planetary Astronomy Program. We wish to thank the IRTF staff for the support of TEXES observations. This work was supported by the Programme National de Planétologie (PNP) of CNRS/INSU, co-funded by CNES. T.K.G. acknowledges support of NASA Grant NNX14AG34G. T.E. and B.B. acknowledge support from CNRS/INSU. T.W. acknowledges support from the University of Versailles-Saint-Quentin and from the Centre National de Recherche Spatiale. M.L. acknowledges support from the Centre National d'Études Spatiales. W.S. acknowledges support from China Scholarship Council Fellowship.

## References

Ando, H., Takagi, M., Fukuhara, T., et al. 2018, J. Geophys. Res., 123, 2270
Ando, H., Takagi, M., Sugimoto, N., et al. 2020, J. Geophys. Res., 125, e06208
Belyaev, D. A., Montmessin, F., Bertaux, J.-L., et al. 2012, Icarus, 217, 740
Bertaux, J.-L., Vandaele, A.-C., Korablev, O., et al. 2007, Icarus, 217, 740
Bézard, B., & ÐeBergh, C. 2012, J. Geophys. Res., 112, E04S07
Bjoraker, G. L., Larson, H. P., Mumma, M. J., et al. 1992 BAAS, 24, 995
Encrenaz, T., Greathouse, T. K., Roe, H., et al. 2012, A&A, 543, A153
Encrenaz, T., Greathouse, T. K., Richter, M. J., et al. 2013, A&A, 559, A65
Encrenaz, T., Greathouse, T. K., Richter, M. J., et al. 2016, A&A, 595, A74
Encrenaz, T., Greathouse, T. K., Marcq, E., et al. 2019, A&A, 623, A70
Encrenaz, T., Greathouse, T. K., Marcq, E., et al. 2020, A&A, 639, A69
Fedorova, A., Korablev, O., Vandaele, A.-C., et al. 2008, J. Geophys. Res., 113, E00B25
Fedorova, A., Marcq, E., Luginin, M., et al. 2016, Icarus, 275, 143
Fukuhara, T., Futagushi, M., Hashimoto, G. L., et al. 2017, Nat. Geosci., 10, 85
Giles, R., Greathouse, T. K., Irwin, P. G., et al. 2022, Icarus, 387, 115187
Kouyama, T., Imamura, T., Taguchi, M., et al. 2017, Geophys. Res. Lett., 44, 12, 098
Krasnopolsky, V. A. 1986, Photochemistry of the Atmospheres of Mars and Venus (New York: Springer-Verlag)
Krasnopolsky, V. A. 2007, Icarus, 191, 25
Krasnopolsky, V. A. 2010, Icarus, 209, 314
Krasnopolsky, V. A., Belyaev, D. A., Gordon, I. A., et al. 2013, Icarus, 224, 57
Lacy, J. H., Richter, M. J., Greathouse, T. K., et al. 2002, PASP, 114, 153
Lee, Y. J., Jessup, K. L., Perez-Hoyos, S., et al. 2019, AJ, 158, 126
Lee, Y. J., Garcia-Munoz, A., Yamazaki, A., et al. 2021, Geophys. Res. Let. 48, e90577
Lefèvre, M., Lebonnois, S., & Spiga, A. 2018, J. Geophys. Res., 123, 2773
Lefèvre, M., Spiga, A., & Lebonnois, S. 2020, Icarus, 335, 113376
Lefèvre, M., Marcq, E., & Lefèvre, F. 2022, Icarus, 386, 115148
Marcq, E., Bertaux, J.-L., Montmessin, F., et al. 2013, Nat. Geosci., 6, 25
Marcq, E., Mills, F. P., Parkinson, C. P. & Vandaele, A. C. 2018, Space Sci. Rev., 214, 10
Marcq, E., Jessup, K. L., Baggio, L., et al. 2020, Icarus, 335, 11368
Markiewicz, W. J., Titov, D. V., Limaye, S. S., et al. 2007, Nature, 145, 633
Mills, F. P., Esposito, L. W., & Yung, Y. K. 2007, in Exploring Venus as a Terrestrial Planet, Geophysical Mongraph Series, 176, 73
Rohlfs, K., & Wilson, T. L. 2004, Tools for Radioastronomy, 4th edn. (Berlin: Springer)
Shao, W. D., Zhang, X., Bierson, C. J., et al. 2020, JGR-Planets, 125, e06195
Titov, D. V., Markiewicz, W. J., Igantiev, N. I., et al. 2012, Icarus, 217, 682
Vandaele, A.-C., Korablev, O., Belyaev, D., et al. 2017a, Icarus, 295, 16
Vandaele, A.-C., Korablev, O., Belyaev, D., et al. 2017b, Icarus, 295, 1
Zhang, K., Liang, M. C., & Mills, F. P. 2012, Icarus, 217, 714
Zasova, L. V., Moroz, V I., Esposito, L. W., & Na, C. Y. 1993, Icarus, 105, 92